Available online at www.sciencedirect.com

ScienceDirect

Proceedings of the Combustion Institute 37 (2019) 2461–2468

Proceedings of the Combustion Institute

www.elsevier.com/locate/proci

Interactions between the premixed flame front and the three-dimensional Taylor–Green vortex

Hao Zhou [a], Jiaping You [a], Shiying Xiong [a], Yue Yang [a,b,*], Dominique Thévenin [c], Shiyi Chen [a,b,d]

[a] *State Key Laboratory for Turbulence and Complex Systems, College of Engineering, Peking University, Beijing 100871, China*

[b] *CAPT and BIC-ESAT, Peking University, Beijing 100871, China*

[c] *Laboratory of Fluid Dynamics and Technical Flows, University of Magdeburg "Otto von Guericke", D-39106 Magdeburg, Germany*

[d] *Department of Mechanics and Aerospace Engineering, South University of Science and Technology of China, Shenzhen 518055, China*

Received 30 November 2017; accepted 12 August 2018
Available online 29 August 2018

Abstract

We study interactions between the premixed flame front and evolving vortices using the vortex-surface field (VSF) and direct numerical simulation of a hydrogen/air premixed flame propagating in a three-dimensional Taylor–Green (TG) flow. The VSF, a Lagrangian-based structure identification method, characterizes the evolution of a vortex surface consisting of vortex lines across the flame front. Compared to the VSF evolution in non-reacting TG flows, the flame has an impact on the evolutionary geometry of vortex surfaces. We find that the vortex surfaces merge into bulky structures without rolling-up of vortex tubes and the transition of the TG flow is suppressed in the burnt region. The vortex surfaces near the flame are expanded with a slight increase of vorticity magnitude owing to the flame-generated positive dilation. The VSF deformation in the burnt region, compared to that in the unburnt region during flow transition, is significantly suppressed near impermeable planes and slightly amplified near the flame front. The effects of flame-induced motion on flame dynamics and geometry are twofold. By comparing the wrinkling of isosurfaces of a progress variable in reacting TG flow and isosurfaces of a passive scalar in non-reacting TG flow, we find that the flame can increase its surface area and the scalar gradient by inducing an additional straining field near the flame front, whereas it can smooth the very sharp scalar structures in non-reacting TG flows under vortex straining near impermeable planes.

Keywords: Flame/vortex interactions; Premixed flames; Vortex-surface field; Direct numerical simulation

1. Introduction

The interaction between premixed flame fronts and vortices plays a crucial role in various practical combustion applications [1]. It is also a fundamen-

* Corresponding author at: State Key Laboratory for Turbulence and Complex Systems, College of Engineering, Peking University, Beijing 100871, China.
E-mail address: yyg@pku.edu.cn (Y. Yang).

https://doi.org/10.1016/j.proci.2018.08.015
1540-7489

tal problem in the interaction between flames and turbulence [2–4]. In general, vortices wrinkle the flame front, which increases the flame surface area and the fuel consumption speed, and very strong vortices can quench the flame [5]. On the other hand, the flame front generates the strong heat release rate and volume expansion, which can reduce the local Reynolds number as relaminarization [6], increase local vorticity, and induce combustion instabilities [7]. Moreover, the flame front can cause the local velocity field to be anisotropic [2,4], so the turbulence theory and models based on the assumption of local isotropy should be scrutinized in turbulent premixed combustion [8].

Most of existing studies on flame/vortex interactions are mainly based on two-dimensional (2D) configurations of a propagating planar flame and a vortex pair or ring [5,7,9–11], in which the major vorticity direction is either parallel or perpendicular to the flame [12]. The flame/vortex interactions in practical applications and turbulence, however, are much more complex than the quasi-2D flame/vortex configurations, the background unsteady vortical flow is generally three-dimensional (3D) and may have laminar-turbulent transitional regions.

Although it is easy to identify a vortex in 2D flows without vortex stretching and twisting using the magnitude of vorticity, there is a lack of ideal vortex-identification methods in 3D flows. Most of former studies identify vortices using Eulerian vortex-identification criteria such as the vorticity magnitude and the others based on the local velocity gradient tensor. These methods can effectively identify the region with strong vorticity or rotational motion, but the vorticity magnitude has large variations near a flame front, so most of the existing methods are not able to identify a continuous, complete vortical structure across the flame and characterize its evolution. Therefore, it appears to be challenging to characterize flame/vortex interactions in 3D configurations.

Alternatively, the vortex-surface field (VSF), whose isosurface is a vortex surface consisting of vortex lines, is developed to tackle the issue of the characterization of evolving vortical structures [13]. This method is rooted in the Helmholtz vorticity theorem, but it can describe the Lagrangian-like evolution of vortex surfaces in variable-density viscous flows with numerical regularization. The VSF method has been applied to incompressible viscous highly-symmetric flow [14], transitional channel flows [15,16], and compressible flows with shocklets [17]. Numerical results on the evolution of VSFs clarify the continuous vortex dynamics in these transitional flows from a Lagrangian perspective in terms of topology and geometry of vortex surfaces.

In the present study, we propose a new direct numerical simulation (DNS) case for interactions of evolving Taylor–Green (TG) vortices [14,18] and flames in a 3D configuration, and extend the VSF from non-reacting flows to reacting flows. The TG vortical flow has a simple initial vorticity field and has a clear transition process from a laminar flow to a turbulent-like flow. The VSF has a Lagrangian-based formalism to characterize the timewise continuous evolution of vortex surfaces in reacting flows. In particular, the VSF can characterize a complete vortical structure consisting of vortex lines across the flame front, which tackles the problem of vortex identification in 3D premixed combustion. Furthermore, we will compare a flame front and a passive scalar interface evolved from the same initial condition to reveal the influence of the flame on scalar structures.

2. Simulation overview

2.1. DNS

We consider a planar premixed H_2/air flame freely propagating in an evolving TG flow. The DNS for flame/vortex interactions is performed in a rectangular domain with sizes $L_x \times L_y \times L_z = 4L \times L \times L$ and $L = 2$ mm on $1024 \times 256 \times 256$ structured uniform grids. All the boundaries are periodic.

The unburnt gas is a lean H_2/air mixture at atmospheric pressure with the equivalence ratio $\Phi = 0.8$. The temperature of the unburnt gas is $T_u = 300$ K and the adiabatic flame temperature is $T_{\mathrm{ad}} = 2177$ K. The flame speed of the initial laminar premixed flame is $S_L = 1.467$ m/s, the flame thermal thickness is $\delta = 0.318$ mm, and the kinematic viscosity of the unburnt mixture is $\nu = 2.05 \times 10^{-5}$ m^2/s.

The unburnt mixture is ignited by two planar laminar flames, which are initially around $x = L_x/2 \pm L/2$ and propagate towards opposite x-directions with the reflectional symmetry respect to $x = L_x/2$. The corresponding initial temperature profile in the computational domain is

$$T(\boldsymbol{x}, t = 0) = T_u + \frac{T_{\mathrm{ad}} - T_u}{2} \times \left[1 - \tanh\left(4\frac{|x - L_x/2| - L/2}{L/2}\right)\right].$$

The Reynolds number in the unburnt region is set as $\mathrm{Re} \equiv u_0 l/\nu = 400$, which is the same as that in the former study of VSFs in incompressible non-reacting TG flows [14], where $u_0 = 25.76$ m/s and $l = L/(2\pi) = 0.318$ mm are characteristic velocity and length scales of the initial TG vortex, respectively. The TG flows at this moderate Re and higher Re have the similar transitional process from a laminar initial flow to a turbulent-like flow. The Damköhler number $\mathrm{Da} \equiv lS_L/(u_0\delta) = 0.057$ is low.

The DNS of flame/TG-vortex interactions is carried out by the highly parallel code 'DINO' [19] which has been used in DNS of turbulent combustion and multiphase flows [20,21]. DINO is a

low-Mach-number, variable-density flow solver using a sixth-order finite difference scheme for spatial discretization and a third-order Runge–Kutta semi-implicit scheme for time advancement. The nine-species detailed mechanism [22] for H_2/air oxidation is used with the reaction rates, thermodynamic and transport properties evaluated by the software package Cantera 1.8. The species diffusion is treated by the Hirschfelder and Curtiss approximation, and the Soret effect is neglected. The time step is set to 12.3 ns, one-thousandth of the characteristic time l/u_0 of the TG flow. All the quantities, e.g., the spatial coordinates $\boldsymbol{x}$, velocity $\boldsymbol{u}$, vorticity $\boldsymbol{\omega}$, and time t, are in dimensionless forms as $\boldsymbol{x}^* = \boldsymbol{x}/l$, $\boldsymbol{u}^* = \boldsymbol{u}/u_0$, $t^* = tu_0/l$, and $\boldsymbol{\omega}^* = \boldsymbol{\omega}l/u_0$ in following expressions, but the asterisks are omitted for clarity. The initial dimensionless velocity of the TG flow is $(\sin x \cos y \cos z, -\cos x \sin y \cos z, 0)$. We remark that the present DNS setup is the most convenient one to directly compare the flame/vortex interaction case and the former VSF study of non-reacting TG flows [14]. The imposed TG initial field leads to local density variations near the flame front, and the total mass in the computational domain is conserved due to TG symmetries.

2.2. VSF

The VSF ϕ_v is defined to satisfy the constraint $\boldsymbol{\omega} \cdot \nabla\phi_v = 0$, so that every isosurface of ϕ_v is a vortex surface consisting of vortex lines [13]. The calculation of VSFs can be implemented as a post-processing step based on a time series of velocity–vorticity fields in DNS. The two-time method is used to solve the evolution equation of VSFs [14,17], which divides each time step into prediction and correction steps. In the prediction step, the temporary VSF ϕ_v^* is evolved in physical time t as

$$\frac{\partial\phi_v^*(\boldsymbol{x},t)}{\partial t} + \boldsymbol{u}(\boldsymbol{x},t)\cdot\nabla\phi_v^*(\boldsymbol{x},t) = 0, \quad t \geq 0 \tag{1}$$

where $\boldsymbol{u}(\boldsymbol{x}, t)$ is the velocity from DNS. The initial VSF [14] for the TG flow is $\phi_{v0} = (\cos 2x - \cos 2y)\cos z$, and periodic boundary conditions are applied. In general, temporary ϕ_v^* deviates from an accurate VSF owing to the breakdown of the Helmholtz vorticity theorem in variable-density viscous flows, so ϕ_v^* is projected onto the desired VSF solution through the correction step. In the correction step, ϕ_v^* is computed in pseudo-time τ at a fixed physical time t as

$$\frac{\partial\phi_v^*(\boldsymbol{x},t)}{\partial\tau} + \boldsymbol{\omega}(\boldsymbol{x},t)\cdot\nabla\phi_v^*(\boldsymbol{x},t;\tau) = 0, \quad 0 \leq \tau \leq T_\tau, \tag{2}$$

which is driven by the frozen vorticity at a fixed physical time with the initial condition $\phi_v(\boldsymbol{x}, t; \tau = 0) = \phi_v^*(\boldsymbol{x}, t)$. Finally, ϕ_v^* in Eq. (1) is updated by $\phi_v(\boldsymbol{x}, t; \tau = T_\tau)$ from Eq. (2) for each physical time step, where T_τ is a pseudo-time period that is typically less than 100 times of the physical time step.

In the numerical implementation of solving Eqs. (1) and (2), integrations in t and τ are marched by the TVD Runge–Kutta scheme. The convection terms are treated by the fifth-order WENO scheme [23]. The numerical diffusion in the WENO scheme serves as a numerical dissipative regularization for removing small-scale, nearly singular scalar structures. The volume-averaged VSF deviation, which quantifies the mean error of a VSF solution, is very small as $\langle|\lambda_\omega|\rangle < 3\%$ during the time period of interest $0 \leq t \leq 6$ in the present study, where $\lambda_\omega \equiv (\boldsymbol{\omega}\cdot\nabla\phi_v)/(|\boldsymbol{\omega}||\nabla\phi_v|)$ denotes the VSF deviation as the cosine of the angle between the vorticity and the gradient of a VSF solution.

In the visualization of vortex surfaces, we display the normalized VSF $\hat{\phi}_v$. It is implicitly determined by $\hat{M}(\hat{\phi}_v = \varphi, t) = \hat{M}(\phi_{v0} = \varphi, t = 0)$ by searching the isocontour values $\hat{\phi}_v = \varphi$ at a given time t and ϕ_{v0} at $t = 0$ which correspond to the same fluid mass $\hat{M}$ [17]. Thus isosurfaces of $\hat{\phi}_v$ with the same isocontour level at different times can have strong time coherence to display the continuous temporal evolution of a particular vortex surface in a variable-density flow.

3. Flame/TG-vortex interactions

3.1. Evolution of the flame front and vortex surfaces

The evolution of flames and vortex surfaces can be considered to be driven by both flame-induced and vortex-induced motions. Without the flame effect, the non-reacting TG flow has been extensively studied [14,18]. It has multiple reflectional and rotational symmetries in a periodic box with nondimensional sizes $(2\pi)^3$. In particular, the planes where x, y, or z is equal to a multiple of π are impermeable. The present combustion DNS has an additional reflectional symmetry respect to the y–z plane at $x = 4\pi$, whereas the propagating flame breaks the original TG symmetries in the x-direction in each half domain. Thus, we will only display the structural evolution in the left half domain within $0 \leq x \leq 4\pi$.

Figure 1 shows the evolution of the isosurfaces of the normalized VSF $\hat{\phi}_v = \pm 0.5$ for vortex surfaces and the isosurface of the progress variable $c \equiv (T - T_u)/(T_{ad} - T_u) = 0.41$ for the flame, which corresponds to the peak heat release rate in the unstrained laminar flame of the unburnt mixture. The VSF isosurface of $\hat{\phi}_v = 0.5$ is color-coded by $|\boldsymbol{\omega}|$, and the isosurface of $\hat{\phi}_v = -0.5$ is in white. The VSF isosurfaces at particular contour levels $\hat{\phi}_v = \pm\varphi$ have very similar dynamics in the unburnt region, but they move in different directions under TG symmetries [18]. Some vortex lines are integrated from points on the surfaces. Since the VSF deviation is very small in this simulation, the vortex lines lie almost on the VSF isosurfaces. In Fig. 1(a),

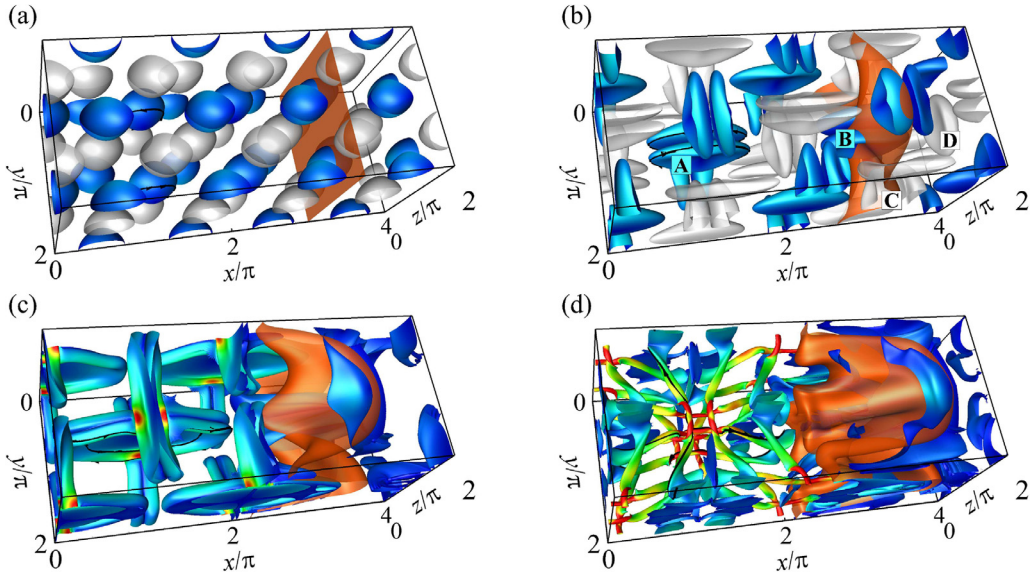

Fig. 1. Evolution of the VSF isosurface in flame/TG-vortex interactions at (a) $t = 0$, (b) $t = 2$, (c) $t = 4$, and (d) $t = 6$. Isosurfaces of $\hat{\phi} = 0.5$ are color-coded by $0 \le |\boldsymbol{\omega}| \le 8$ from blue through green to red. Some vortex lines are integrated and plotted on the isosurfaces. Isosurfaces of $\hat{\phi} = -0.5$ are translucent and in white, and they are not shown in (c) and (d) for clarity. The translucent, orange isosurface of $c = 0.41$ represents the flame front (propagating from right to left). Typical vortex pairs for further analysis are labeled by capital letters in (b). (For interpretation of the references to color in this figure legend, the reader is referred to the web version of this article.)

all the blob-like vortex surfaces are identical at $t = 0$.

In the unburnt region around $x < 2\pi$, vortex surfaces are almost not affected by the flame, so their evolution is very similar to that in non-reacting TG flows [14]. The vortex surfaces are stretched and approach to each other at $t = 2$ in Fig. 1(b), and then they merge together as vortex reconnection during $3 \le t \le 4$ at impermeable planes in Fig. 1(c). The edge of the merged vortex surface is rolled up into vortex tubes with significant vorticity intensification, and the tubes are persistently stretched and twisted at $t = 6$ to reach a nearly turbulent state in Fig. 1(d). It is noted that the vortex tubes at higher Re show more obvious helical geometry and generate more intense small-scale velocity fields [14], but they have the same topology and generation mechanism as in the present study.

In contrast, the strong heat release rate in the flame causes the surge of local temperature and viscosity in the burnt region around $x > 3\pi$. The local Re is reduced from 400 in the unburnt region to 16.4 in the burnt region. As a result, the transition from laminar flow to turbulent-like flow is suppressed as relaminarization, and the rolling-up of vortex tubes after $t = 4$ is not observed. At $t = 6$, the characteristic length scale of thin, twisted vortex tubes with high $|\boldsymbol{\omega}|$ in the unburnt region is much smaller than bulky vortical structures with low $|\boldsymbol{\omega}|$ in the burnt region. In order to obtain the VSF at a full turbulent-like state in the unburnt region and with rolling-up of vortex tubes at Re > 100 [14] in the burnt region, we would need to simulate the TG flow at Re $\ge$ 2500 on grid points $4096 \times 1024 \times 1024$ for studying flame/turbulence interactions.

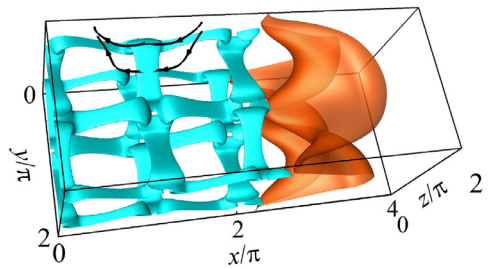

Fig. 2. Isosurfaces of $|\boldsymbol{\omega}| = 4$ (light blue) and $c = 0.41$ (orange) at $t = 4$. Some vortex lines are integrated and plotted on the isosurface of $|\boldsymbol{\omega}|$. (For interpretation of the references to color in this figure legend, the reader is referred to the web version of this article.)

It has been demonstrated that the isosurface of the vorticity magnitude and other Eulerian vortex-identification criteria are very different from vortex surfaces owing to the significant misalignment of their isosurfaces and nearby vortex lines (also see Fig. 2), and the evolution of the Eulerian vortical structures cannot be explained by the Helmholtz vorticity theorem [14]. By comparing visualizations

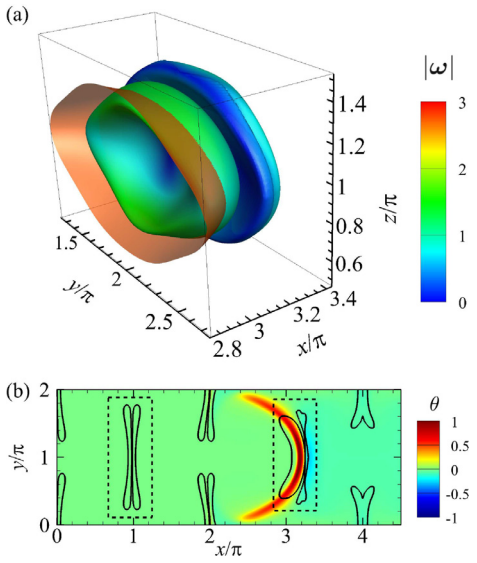

Fig. 3. Different volume changes of vortex surfaces at $t = 3$. (a) The isosurface of $\hat{\phi} = -0.5$ (vortex pair C) color-coded by $|\boldsymbol{\omega}|$ and isosurface of $c = 0.41$ in orange. (b) The contour of θ and contour line of $\hat{\phi} = -0.5$ on the x–y plane at $z = \pi$. (For interpretation of the references to color in this figure legend, the reader is referred to the web version of this article.)

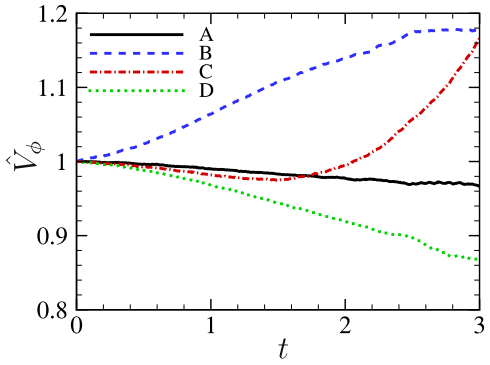

Fig. 4. Evolution of the normalized volume of four typical vortex pairs labeled in Fig. 1(b), where pair A is in the unburnt region, pairs B and C are near the flame front, and pair D is in the burnt region.

of the VSF in Fig. 1(c) and $|\boldsymbol{\omega}|$ in Fig. 2, we find that the isosurface of $|\boldsymbol{\omega}| = 4$ suddenly disappears around $x > 2\pi$ owing to diminishing $|\boldsymbol{\omega}|$ across the flame front, so it is challenging to characterize how the flame influences continuous vortex dynamics using the Eulerian vortical structures. Moreover, we fix $\hat{\phi}_v = \pm 0.5$ in the VSF visualization and display strong temporal coherence in the evolution of vortex surfaces in Fig. 1, unlike the subjective selection of varied isocontour levels at different times in most of vortex-identification methods.

3.2. *Effects of the flame on vortex surfaces*

Compared to the fully unburnt and burnt regions, the flame and vortex surfaces have strong interactions in the flame brush which is located around $x = 3\pi$ at $t = 0$ and spanned over $2\pi < x < 4\pi$ at later times. The flame has an impact on the geometry of nearby vortex surfaces, and the straining motion induced by vortices wrinkles the flame at the mean time. Figure 3(a) shows a curved flame as the isosurface of $c = 0.41$, between a pair of vortex surfaces as the isosurface of $\hat{\phi}_v = -0.5$ at $t = 3$, which is evolved from the vortex pair labeled by 'C' in Fig. 1(b). Figure 3(b) shows the contour of the nondimensional dilatation $\theta \equiv \nabla \cdot \boldsymbol{u}$ on the x–y plane at $z = \pi$, which is formed by the strong heat release rate and large density gradient near the flame. By comparing VSF isocontour lines in the two dashed rectangles, we find that the strong positive dilation adjacent to the flame significantly expand the vortex surface and increase local $|\boldsymbol{\omega}|$, while the weak negative dilatation on the burnt side slightly shrinks the vortex surface and reduce $|\boldsymbol{\omega}|$.

The volume changes of four typical pairs of vortex surfaces, which are labeled in Fig. 1(b), are quantified by the normalized volume $\hat{V}_\phi \equiv V_\phi(\hat{\phi}_v = \varphi)/V_0(\hat{\phi}_{v0} = \varphi)$ in Fig. 4, where V_0 is the initial volume of the fluid enclosed in the isosurface of $\hat{\phi}_{v0} = \varphi$ for each vortex pair. Thus $\hat{V}_\phi > 1$ and $\hat{V}_\phi < 1$ characterize volume expansion and shrinkage of a vortex pair, respectively. We find that $\hat{V}_\phi$ is almost unaltered for vortex pair A in the unburnt region, while it is decreased for pair D in the burnt region. Pairs B and C near the flame have notable overall volume expansion.

Figure 5(b) displays that a pair of merging vortex surfaces, which is evolved from vortex pair B in Fig. 1(b), crosses the frame front at $t = 4$. As shown in the dashed rectangle in Fig. 5(b), the geometry of the counterpart of vortex pair B in the unburnt region is symmetric respect to $x = \pi$, while the symmetry is broken by the flame. Since the burnt region has lower local Re, vortex surfaces on the burnt side merge together and exhibit less geometric deformation than those on the unburnt side.

It is interesting that the deformation of vortex surfaces around $x = 2\pi$ in Fig. 5(a) is even stronger than its counterpart around $x = 0$ in the unburnt region. Figure 5(b) shows that strong Λ-like positive dilation is generated near the flame front. Thus vortex surfaces are expanded along the positive dilatation on the unburnt side of the flame, while they are shrunk on the burnt side. The flame-induced expansion of vortex surfaces is partially blocked by the impermeable plane at $x = 2\pi$ defined in the non-reacting TG flow, which causes the rolling-up of the temperature structure (not shown) and forms a weak, bow-like positive dilation near

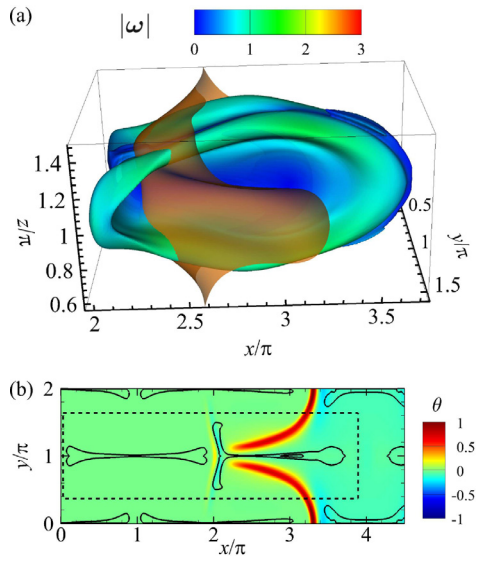

Fig. 5. Different deformation of vortex surfaces at $t = 4$. (a) The isosurface of $\hat{\phi} = 0.5$ (vortex pair B) color-coded by $|\boldsymbol{\omega}|$ and the isosurface of $c = 0.41$ in orange. (b) The contour of θ and contour line of $\hat{\phi} = 0.5$ on the x–y plane at $z = \pi$. (For interpretation of the references to color in this figure legend, the reader is referred to the web version of this article.)

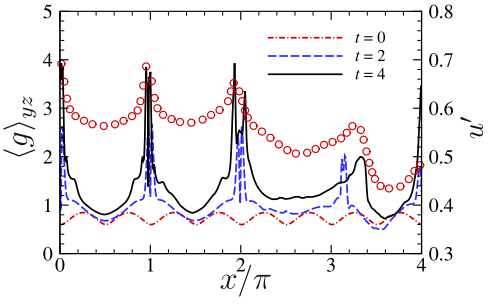

Fig. 6. Deformation of vortex surfaces and rms velocity fluctuation along the x-direction (lines: $\langle g \rangle_{yz}$ at different times; symbols: u' at $t = 4$).

$x = 2\pi$. Thus the left edge of vortex surfaces of pair B are rolled up to form a nose-like structure with large curvatures. It appears that the effect of flames on vortex evolution increases the local velocity anisotropy, which supports the relevant statistical study in flame/turbulence interactions [2,4,8].

The overall deformation of vortex surfaces along the x-direction is quantified by averaged $g \equiv |\nabla \phi_v|$ at different x in Fig. 6. The profile of $\langle g \rangle_{yz}$ is a function of $\cos 4x$ at $t = 0$, and in general g is increased with time owing to vortex-induced straining, where $\langle \cdot \rangle_{yz}$ denotes the average over the y–z plane. In non-reacting TG flows or in the unburnt region, $\langle g \rangle_{yz}$ has peak values near impermeable planes as shown as flatten vortex surfaces in Fig. 1(b) and (c) at $t = 2$ and 4. Nevertheless, the flame breaks the periodicity and symmetries at $x > 2\pi$, which destructs the impermeable plane at $x = 3\pi$ and significantly reduces local Re. Thus $\langle g \rangle_{yz}$ near $x = 3\pi$ in the burnt region is much smaller than its counterpart in the unburnt region, which is consistent with the observation on the vortex deformation in Figs. 1, 3, and 5. The flame-induced deformation on the right of $x = 2\pi$ in Fig. 5 is also quantified as the secondary peak of $\langle g \rangle_{yz}$ around $x = 2.1\pi$ in Fig. 6. In addition, we find that the VSF deformation is highly correlated to the rms velocity fluctuation u' at $t = 4$ during transition.

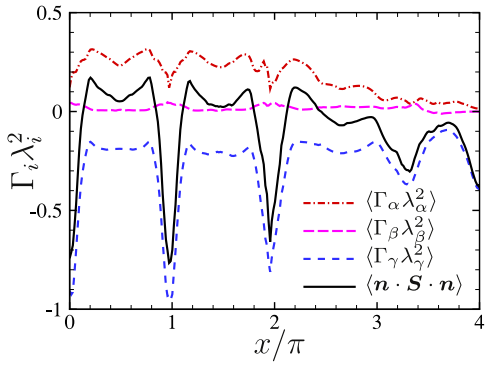

Fig. 7. Decomposition of the straining effect on VSF deformation at $t = 4$.

Since the VSF deformation is close to the deformation of a Lagrangian tracer field at early times before significant vortex reconnection [13], the evolution equation of g can be approximated by [24]

$$\mathrm{D}g/\mathrm{D}t = -(\boldsymbol{n} \cdot \boldsymbol{S} \cdot \boldsymbol{n})g, \tag{3}$$

where $\boldsymbol{S}$ is the rate-of-strain tensor and $\boldsymbol{n} \equiv \nabla \phi_v / g$ is the normal of the vortex surface. Let the principal strain rates for $\boldsymbol{S}$ be Γ_α, Γ_β, and Γ_γ, with the specified order $\Gamma_\alpha \geq \Gamma_\beta \geq \Gamma_\gamma$ and corresponding unit vectors along the principal axes of strain $\boldsymbol{e}_\alpha$, $\boldsymbol{e}_\beta$, and $\boldsymbol{e}_\gamma$. We decompose the averaged straining effect on VSF into $\langle \boldsymbol{n} \cdot \boldsymbol{S} \cdot \boldsymbol{n} \rangle = \langle \Gamma_\alpha \lambda_\alpha^2 \rangle + \langle \Gamma_\beta \lambda_\beta^2 \rangle + \langle \Gamma_\gamma \lambda_\gamma^2 \rangle$, where the alignment vector $\lambda_i = \boldsymbol{n} \cdot \boldsymbol{e}_i$ is defined as the cosine of the angle between $\boldsymbol{n}$ and $\boldsymbol{e}_i$. In general, negative $\langle \boldsymbol{n} \cdot \boldsymbol{S} \cdot \boldsymbol{n} \rangle$ in Fig. 7 increases g implied by Eq. (3). The major contribution comes from $\langle \Gamma_\gamma \lambda_\gamma^2 \rangle$ indicating the preferential alignment between $\boldsymbol{n}$ and the most compressive strain direction, which is consistent with the finding in non-reacting turbulent flows [24]. In the burnt region, the flame significantly suppresses $\langle \Gamma_\alpha \lambda_\alpha^2 \rangle$ by weakening the alignment λ_α between $\boldsymbol{n}$ and the most extensional strain direction (not shown), so the straining effect and VSF deformation in the burnt region can be slightly larger than the counterpart

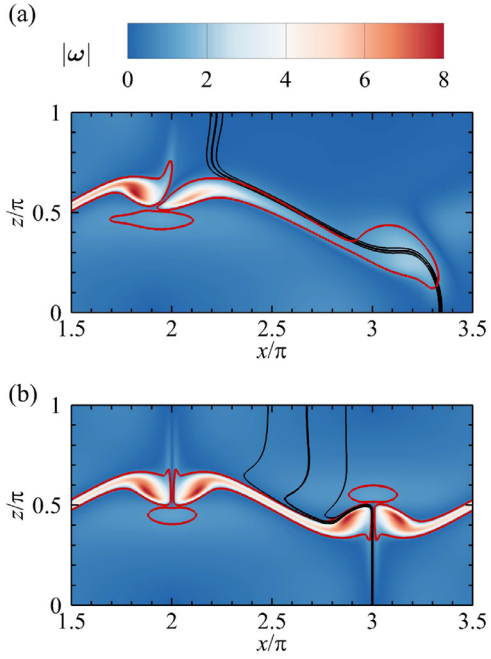

Fig. 8. Contour lines of $c = 0.36, 0.41, 0.46$ (from left to right, black) and $|\boldsymbol{\omega}| = 1$ (red) and the contour of $|\boldsymbol{\omega}|$ on the x–z plane at $y = \pi$ and at $t = 4$, (a) flame/TG-vortex interactions, (b) non-reacting TG flow. (For interpretation of the references to color in this figure legend, the reader is referred to the web version of this article.)

in the unburnt region except for the region close to impermeable planes in Figs. 6 and 7.

3.3. Wrinkling of the flame front

The flame can relaminarize a vortical flow and create vorticity near its front [6]. These influences on the flow field also feedback on its own dynamics and geometry. Figure 8(a) shows a curved flame front as black contour lines of $c = 0.41$ and $c = 0.41 \pm 0.05$ along with the contour of $|\boldsymbol{\omega}|$ on the x–z plane at $y = \pi$ and at $t = 4$. Here, we only show the bottom half owing to the reflectional symmetry respect to $z = \pi$. The flame wrinkling is caused by vortex-induced straining and flame-induced expansion and propagation. In order to isolate the former effect, we also perform a separate DNS for the evolution of c in a cold and non-reacting TG flow at the same $\mathrm{Re} = 400$, where c becomes a passive scalar with the same initial value of the progress variable in the flame case at $t = 0$. Then we compare contour lines of the passive scalar in Fig. 8(b) with those of the progress variable as an active scalar in the flame in Fig. 8(a).

The overall deformation of flame and scalar surfaces along the x-direction is quantified by plane-averaged $\Sigma' \equiv |\nabla c|$ at different x in Fig. 9. Profiles of $\langle \Sigma' \rangle_{yz}$ for both surfaces are the same

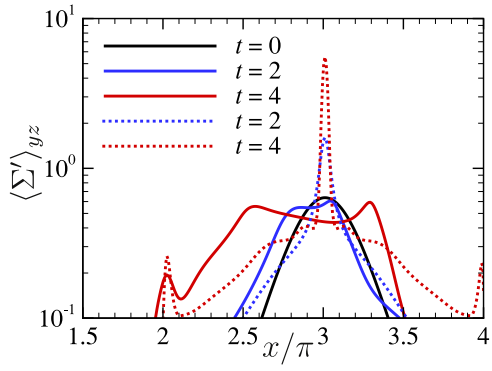

Fig. 9. Deformation of isosurfaces of c (solid lines: progress variable in the flame; dashed lines: passive scalar in the non-reacting flow).

as a transform of $\mathrm{sech}^2 x$ at $t = 0$. In the non-reacting flow, the symmetric $\langle \Sigma' \rangle_{yz}$ is spread over $2\pi \le x \le 4\pi$, while it is also gradually concentrated at the impermeable plane at $x = 3\pi$ under vortex straining. In contrast, the profile of $\langle \Sigma' \rangle_{yz}$ is skewed to the unburnt side, because the large heat release rate near the propagating flame front increases the local temperature gradient. In general, $\langle \Sigma' \rangle_{yz}$ of the flame is larger than $\langle \Sigma' \rangle_{yz}$ of the passive scalar except near impermeable planes.

The wrinkling of the flame front in the TG vortex significantly changes scalar structures of c and nearby vorticity fields. Comparing contour lines of c in Fig. 8, the passive surface is confined between two impermeable planes at $x = 2\pi$ and 3π, whereas the flame is stretched over the impermeable planes. The flame front is stretched via tangential strain-rate and propagation-curvature effects. Since the self-propagation speed of the initially planar flame is much smaller than the TG vortex straining speed as $S_L/u_0 = 0.057$, the increase of the flame surface is primarily due to the tangential strain-rate. Implied by Figs. 8 and 9, the flame induces an additional velocity gradient near its front, which increases the flame surface area and the corresponding fuel consumption speed. Since the flame-induced motion affects scalar structures and subsequent mixing, the flame-induced mixing should be considered in mixing models of the PDF-like modeling approach [25]. Comparing contours of $|\boldsymbol{\omega}|$ in Fig. 8, the vorticity magnitude is diminished along the flame. On the other hand, the flame-generated vorticity, which manifests as the slight expansion of the contour lines of $|\boldsymbol{\omega}| = 1$ near highly-curved portions of the flame front around $x = 1.9\pi$ and $x = 3.3\pi$, is relatively small.

4. Conclusions

We investigate interactions between the premixed flame front and vortex surfaces in a 3D TG

flow at Re = 400 using VSF and DNS. The unburnt H_2/air mixture with $\Phi = 0.8$ in the TG flow is initially ignited near the center of the computational domain, then propagating premixed flames interact with evolving TG vortices. The VSF, a Lagrangian-based structure identification method, is applied to flame/vortex interactions. The two-time method is used to calculate VSFs with very small VSF deviation $\langle|\lambda_\omega|\rangle < 3\%$.

The evolution of the flame front and vortex surfaces is visualized by isosurfaces of the progress variable $c = 0.41$ and the normalized VSF $\tilde{\phi}_v = \pm 0.5$, respectively. Compared to the VSF evolution in non-reacting TG flows, the flame breaks the periodicity and symmetries in the x-direction and has an impact on the vorticity magnitude and evolutionary geometry of vortex surfaces. We find that the vortex surfaces merge into bulky structures without rolling-up of vortex tubes after $t = 4$ in the burnt region with diminishing vorticity magnitude, while they are almost not affected in the unburnt region. The vortex surfaces near the flame front are expanded owing to the flame-generated positive dilation at $t = 3$. Compared to the VSF deformation in the unburnt region, g is significantly suppressed near impermeable planes and slightly amplified near the flame front in the burnt region at $t = 4$.

The effects of flame-induced motion on flame dynamics and geometry are twofold. By comparing the wrinkling of the flame, characterized by the isosurface of a progress variable, in reacting TG flow and the isosurface of a passive scalar in non-reacting TG flow, we find that the flame can increase its surface area and the scalar gradient by inducing an additional straining field near the flame front, whereas it can smooth the very sharp scalar structures in non-reacting TG flows under vortex straining near impermeable planes.

The present study demonstrates that the VSF method is applicable to more complex turbulent combustion, e.g., it can be applied to investigate flame/turbulence interactions and elucidate the local anisotropy near the flame front in turbulent premixed combustion.

Acknowledgments

We gratefully acknowledge the University of Magdeburg for providing the DINO code used in this work, and C. Chi for the help on code usage. This work has been supported in part by the National Natural Science Foundation of China (Grant Nos. 91541204 and 11522215).

References

[1] P.H. Renard, D. Thévenin, J.C. Rolon, S. Candel, *Prog. Energy Combust. Sci.* 26 (2000) 225–282.
[2] P.E. Hamlington, A.Y. Poludnenko, E.S. Oran, *Phys. Fluids* 23 (2011) 125111.
[3] A.J. Aspden, M.S. Day, J.B. Bell, *J. Fluid Mech.* 680 (2011) 287–320.
[4] B. Bobbitt, G. Blanquart, *Phys. Fluids* 28 (2016) 015101.
[5] T. Poinsot, D. Veynante, S. Candel, *J. Fluid Mech.* 228 (1991) 561–606.
[6] T. Poinsot, D. Veynante, *Theoretical and Numerical Combustion*, second, Edwards, 2005.
[7] C.J. Mueller, J.F. Driscoll, D.L. Reuss, M.C. Drake, M.E. Rosalik, *Combust. Flame* 112 (1998) 342–346.
[8] H. Kolla, E.R. Hawkes, A.R. Kerstein, N. Swaminathan, J.H. Chen, *J. Fluid Mech.* 754 (2014) 456–487.
[9] D.S. Louch, K.N.C. Bray, *Combust. Flame* 125 (2001) 1279–1306.
[10] S. Lapointe, B. Bobbitt, G. Blanquart, *Proc. Combust. Inst.* 35 (2015) 1033–1040.
[11] F. Thiesset, F. Halter, C. Bariki, et al., *J. Fluid Mech.* 831 (2017) 618–654.
[12] S. Kadowaki, T. Hasegawa, *Prog. Energy Combust. Sci.* 31 (2005) 193–241.
[13] Y. Yang, D.I. Pullin, *J. Fluid Mech.* 661 (2010) 446–481.
[14] Y. Yang, D.I. Pullin, *J. Fluid Mech.* 685 (2011) 146–164.
[15] Y. Zhao, Y. Yang, S. Chen, *J. Fluid Mech.* 802 (2016) R4.
[16] S. Xiong, Y. Yang, *J. Comput. Phys.* 339 (2017) 31–45.
[17] N. Peng, Y. Yang, *Phys. Rev. Fluids* 3 (2018) 013401.
[18] M.E. Brachet, D.I. Meiron, S.A. Orszag, B.G. Nickel, R.H. Morf, U. Frisch, *J. Fluid Mech.* 130 (1983) 411–452.
[19] A. Abdelsamie, G. Fru, T. Oster, F. Dietzsch, G. Janiga, D. Thévenin, *Comput. Fluids* 131 (2016) 123–141.
[20] A. Abdelsamie, D. Thévenin, *Proc. Combust. Inst.* 36 (2017) 2493–2502.
[21] R. Schießl, V. Bykov, U. Maas, A. Abdelsamie, D. Thévenin, *Proc. Combust. Inst.* 36 (2017) 673–679.
[22] J. Li, Z. Zhao, A. Kazakov, F. Dryer, *Int. J. Chem. Kinet.* 36 (2004) 566–575.
[23] G.S. Jiang, C.W. Shu, *J. Comput. Phys.* 126 (1996) 202–228.
[24] Y. Yang, D.I. Pullin, I. Bermejo-Moreno, *J. Fluid Mech.* 654 (2010) 233–270.
[25] M. Kuron, Z. Ren, E.R. Hawkes, et al., *Combust. Flame* 177 (2017) 171–183.